Mechanical Erosion Modeling of TPS Materials

Sergio Fraile Izquierdo*, Jeremie B. E. Meurisse*, Georgios Bellas Chatzigeorgis*, Nagi N. Mansour*
Analytical Mechanics Associates, Inc. at NASA Ames Research Center, Moffett Field, California

This work describes the development of a model that accounts for the additional total surface recession in Thermal Protection Systems materials as a result of mechanical erosion due to high shear conditions during atmospheric entry. A computational solid mechanics capability module was integrated within the Porous material Analysis Toolbox based on OpenFOAM, PATO. The mechanical erosion was modeled in three steps: first, the implemented stress analysis solver module computes the stress and the displacement fields for orthotropic materials using the wall shear stress tensor as a boundary condition; then, regions on the surface where the stress meets the failure criteria are identified; and last, the mesh is moved accordingly to remove the failed material. The outcome is a model of the total recession of the material due to surface chemistry and mechanical erosion. Results will be included in the final paper after verifying and completing the study.

I. Introduction

For ablative thermal protection materials, the term mechanical erosion, also known as spallation, refers to the physical ejection of solid particles from the ablating surface. This results in an increased total surface recession and must be taken into account for heat shield modeling. This phenomenon has been extensively studied in the literature over the last decades by numerous authors [1–6]. Three mechanisms have been identified as the main causes: the shear stress induced by the flow, the normal stress induced by pyrolysis gas build-up, and the thermal stress induced by the material's temperature field. How much each of these mechanisms and factors contribute to the spallation process is not well understood. There are also factors harder to quantify that may also contribute: the impact of ejected particles back on the surface, the abrasion from the particles removed upstream, and the increased surface roughness. The model described in this work focuses on modeling the shear stress induced on the material by the flow field. Future development efforts will include the other two mechanisms.

This paper describes the development of a modeling framework to account for mass removal due to mechanical erosion of Thermal Protection Systems (TPS) materials during high-shear entry conditions. This work was performed as part of NASA's Entry Systems Modeling (ESM) project to evaluate potential risks associated with high-shear environments during atmospheric entry of future missions. The goal is to evaluate, using state-of-the-art modeling tools, if mechanical erosion could lead to excessive material recession during specific atmospheric return scenarios from beyond low Earth orbit. To assess the mechanical behavior of the TPS materials, a stress analysis solver was added to the Porous material Analysis Toolbox based on OpenFOAM (PATO) [7–9] and then coupled with the entry material response physics already implemented in the software: ablation, heat conduction, multi-phase pyrolysis, finite-rate chemistry, and species conservation. The coupling of all solvers enables the simulation of the total recession of TPS materials due to surface chemistry and mechanical erosion.

The following section describes the methodology used to model mechanical erosion due to high shear. A brief overview of the PATO software and the material response models can be found in Section II.A. Governing equations, numerical methods, and verification cases for the solid mechanics solver are described in Section II.B. The failure criteria model used as a first approach to locate the failing regions is described in Section II.C, and the mass removal model developed to compute the mass loss and move the mesh to account for the failed material is summarized in Section II.D. Section III will present the results of a TPS material test case selected to analyze its mechanical behavior during atmospheric entry. And Section IV will summarize the insights from this work.

*Entry Systems and Technology Division

II. Methodology

A. Material Response Models

The computational model is a generic mass and heat transfer model for porous reactive materials containing several solid phases and a single gas phase. The model includes solid pyrolysis, pyrolysis species injection in the gas phase, heterogeneous reactions between the solid phases and the gas phase, and homogeneous reactions in the gas phase. The chemistry models are integrated into a macroscopic model derived by volume-averaging the governing equations for conserving solid mass, gas mass, momentum, and energy. This generic model is implemented in PATO, a C++ top-level module of OpenFOAM, an open-source computational fluid dynamics software. The open-source library Mutation++, released by the von Karman Institute for Fluid Dynamics, is dynamically linked to compute equilibrium chemistry compositions, and thermodynamic and transport properties [10]. Gas surface interactions are modeled using equilibrium chemistry models preferred for "conservative" design due to lack of data and validated finite-rate chemistry models.

The governing equations of the equilibrium model include the conservation of mass, Darcy's law, and conservation of energy in the material. They are stated here for convenience. These equations are consistent with the single temperature volume averaged [11] governing equations:

$$\partial_t\left(\chi_{i,j}\right) = (1-\chi_{i,j})^{m_{i,j}}\, T^{n_{i,j}}\, \mathcal{A}_{i,j} \exp\left(-\mathcal{E}_{i,j}/\mathcal{R}T\right), \quad i \in N_\mathrm{s}, \quad j \in P_i, \tag{1a}$$

$$\partial_t\left(\epsilon_\mathrm{g}\rho_\mathrm{g}\right) + \partial_\mathbf{x}\cdot\left(\epsilon_\mathrm{g}\rho_\mathrm{g}\mathbf{v}_\mathrm{g}\right) = \Pi, \tag{1b}$$

$$\mathbf{v}_\mathrm{g} = -\frac{1}{\epsilon_\mathrm{g}\mu_\mathrm{g}}\underline{\underline{\mathbf{K}}}\cdot\partial_\mathbf{x}p_\mathrm{g}, \tag{1c}$$

$$\partial_t\left(\rho_\mathrm{t}e_\mathrm{t}\right) + \partial_\mathbf{x}\cdot\left(-\underline{\underline{\mathbf{k}}}\cdot\partial_\mathbf{x}T\right) + \partial_\mathbf{x}\cdot\left(\epsilon_\mathrm{g}\rho_\mathrm{g}h_\mathrm{g}\mathbf{v}_\mathrm{g}\right) = 0, \tag{1d}$$

where $\chi_{i,j}$ is the advancement of pyrolysis reaction j within phase i, $[m,n,\mathcal{A},\mathcal{E}]_{i,j}$ are the Arrhenius law parameters, N_s is the number of solid phases, P_i is the number of subphases in phase i, ϵ_g is the porosity, ρ_g is the gaseous density, $\mathbf{v}_\mathrm{g}$ is the gaseous velocity, Π is the total pyrolysis gas production rate, μ_g is the gaseous viscosity, $\underline{\underline{\mathbf{K}}}$ is the permeability, p_g is the pressure, e_t is the total specific energy, $\underline{\underline{\mathbf{k}}}$ is the thermal conductivity, T is the temperature, and h_g is the gaseous specific enthalpy.

B. Stress Analysis Solver

Considering an arbitrary body of volume Ω, bounded by surface Γ with unit normal $\boldsymbol{n}$, the conservation of linear momentum in strong integral form is given by:

$$\overbrace{\frac{\mathrm{D}}{\mathrm{D}t}\int_\Omega \rho\,\boldsymbol{\upsilon}\,\mathrm{d}\Omega}^{\text{Inertia}} = \overbrace{\oint_\Gamma \boldsymbol{n}\cdot\boldsymbol{\sigma}\,\mathrm{d}\Gamma}^{\text{Surface Forces}} + \overbrace{\int_\Omega \rho\,\boldsymbol{b}\,\mathrm{d}\Omega}^{\text{Body Forces}}. \tag{2}$$

where $\boldsymbol{\upsilon}$ is the velocity vector, $\boldsymbol{\sigma}$ is the Cauchy or engineering stress tensor, ρ is the density, and $\boldsymbol{b}$ is the body force per unit mass. The conservation of linear momentum is a generalization of Newton's second law of motion, which states that the rate of change of the total linear momentum of a body is equal to the sum of all the forces acting on the body. In addition, the conservation of angular momentum is guaranteed thanks to the symmetry of the Cauchy stress tensor [12].

The constitutive relation of solid material is the equation that relates the material stresses with the material strains. In this document, all material deformations are assumed small and follow linear elasticity. Thermal effects are accounted for, but plastic and viscous effects are neglected. With these assumptions, the relationship between stress and strain is governed by the generalized Hooke's theory of elasticity [13]:

$$\mathbf{T} = \mathbf{C} : (\mathbf{E} - \mathbf{A}\Delta T) \tag{3}$$

where $\mathbf{T}$ is the Cauchy stress tensor, $\mathbf{C}$ the fourth-order elastic stiffness tensor, the operator : signifies a double dot product, $\mathbf{E}$ the strain tensor, and $\mathbf{A}$ the coefficient of thermal expansion. Since this model assumes small strains and small rotations in the deformed body, the strain tensor can be defined in terms of the displacement gradient:

$$\mathbf{E} = \text{symm}[\nabla \boldsymbol{u}] = \frac{1}{2}(\nabla \boldsymbol{u} + \nabla \boldsymbol{u}^T) \tag{4}$$

The implementation of the solver in PATO is valid for homogeneous materials and orthotropic materials with unique and independent mechanical properties in three mutually perpendicular directions. For orthotropic cases, the 81 components of the elastic stiffness tensor, $\mathbf{C}$, can be reduced to nine independent material parameters. As a result, the generalized Hooke's law, Eq. (3), can be rewritten for orthotropic thermo-linear elastic materials in Voigt 6×6 matrix notation as follows [14]:

$$\begin{bmatrix} \sigma_{11} \\ \sigma_{22} \\ \sigma_{33} \\ \sigma_{12} \\ \sigma_{23} \\ \sigma_{31} \end{bmatrix} = \begin{bmatrix} A_{11} & A_{12} & A_{31} & 0 & 0 & 0 \\ A_{12} & A_{22} & A_{23} & 0 & 0 & 0 \\ A_{31} & A_{23} & A_{33} & 0 & 0 & 0 \\ 0 & 0 & 0 & A_{44} & 0 & 0 \\ 0 & 0 & 0 & 0 & A_{55} & 0 \\ 0 & 0 & 0 & 0 & 0 & A_{66} \end{bmatrix} \begin{bmatrix} \epsilon_{11} - \alpha_{11}\Delta T \\ \epsilon_{22} - \alpha_{22}\Delta T \\ \epsilon_{33} - \alpha_{33}\Delta T \\ \epsilon_{12} \\ \epsilon_{23} \\ \epsilon_{31} \end{bmatrix} \tag{5}$$

where the orthotropic stiffness coefficients, A_{ij}, are related to the Young's moduli, E_i, Poisson's ratios, ν_{ij}, and shear moduli, G_{ij}, by:

$$\begin{aligned} &A_{11} = \frac{1 - \nu_{23}\nu_{32}}{A_0 E_2 E_3}, \quad A_{22} = \frac{1 - \nu_{13}\nu_{31}}{A_0 E_1 E_3}, \quad A_{33} = \frac{1 - \nu_{21}\nu_{12}}{A_0 E_2 E_1}, \\ &A_{12} = \frac{\nu_{12} - \nu_{32}\nu_{13}}{A_0 E_1 E_3}, \quad A_{23} = \frac{\nu_{23} - \nu_{21}\nu_{13}}{A_0 E_1 E_2}, \quad A_{31} = \frac{\nu_{31} - \nu_{21}\nu_{32}}{A_0 E_2 E_3}, \\ &A_{44} = 2G_{12}, \quad A_{55} = 2G_{23}, \quad A_{66} = 2G_{31}, \\ &A_0 = \frac{1 - \nu_{12}\nu_{21} - \nu_{23}\nu_{32} - \nu_{13}\nu_{31} - 2\nu_{21}\nu_{32}\nu_{13}}{E_1 E_2 E_3} \end{aligned} \tag{6}$$

The three Young's moduli E_1 E_2 E_3 correspond to the elastic moduli in the global x, y, and z directions. The Poisson's ratios ν_{ij} correspond to the strain in the j direction due to a strain in the i direction. Poisson's ratios ν_{ij} and ν_{ji} are related by the relation $\frac{\nu_{ij}}{E_i} = \frac{\nu_{ji}}{E_j}$. The shear modulus G_{ij} corresponds to the plane ij plane and follows the relation $G_{ij} = G_{ji}$.

Employing Reynold's transport theorem, the conservation of linear momentum, Eq. (2), can be rewritten by replacing the total derivative by a partial derivative as follows:

$$\frac{\partial}{\partial t}\int_\Omega \rho\, \upsilon \, \mathrm{d}\Omega + \oint_\Gamma \rho \upsilon \, [n \cdot (\upsilon - \upsilon_\Gamma)] \, \mathrm{d}\Gamma = \oint_\Gamma n \cdot \sigma \, \mathrm{d}\Gamma + \int_\Omega \rho \, b \, \mathrm{d}\Omega \tag{7}$$

where $\boldsymbol{\upsilon}_\Gamma$ is the velocity of the control volume surface Γ. In solid mechanics, a Lagrangian approach is typically adopted for the analysis of solids, which means that the velocity of the material is assumed to be equal to the velocity of the domain: $\upsilon - \upsilon_\Gamma = 0$. As a result, the second integral of the left-hand side of Eq. (7), which represents the convection term, drops out of the equation:

$$\frac{\partial}{\partial t}\int_{\Omega_0} \rho \frac{\partial u}{\partial t} \, \mathrm{d}\Omega_0 = \oint_{\Gamma_0} n_0 \cdot \sigma \, \mathrm{d}\Gamma_0 + \int_{\Omega_0} \rho \, b \, \mathrm{d}\Omega_0 \tag{8}$$

The procedures by which equation terms are discretized and the solution algorithm implemented are handled internally by OpenFOAM [15], validation cases, and additional implementation details will be included in the final paper.

C. Stress-based Failure Criteria Model

The stresses obtained by solving the governing equations described in Sec. II.B may lead to material failure and mechanical erosion, particularly near the surface of TPS materials, where the oxidized fibers have thinned and are mechanically weaker. The relative importance of mechanical erosion compared to the rest of the ablation processes is still an unresolved problem. Recent experimental campaigns and numerical simulations [16, 17] are attempting to answer this question. Numerical investigations of mechanical erosion in the branch of hypersonics are still limited to predicting failure at a fiber level [18], with the objective of providing an understanding of the failure mechanisms. In the current approach, the developed model predicts surface recession rates at the macro-scale in two steps. Based on a failure model, the first step determines the material regions where the stress as computed with the stress analysis solver exceeds a failure threshold. The second step translates the failing regions into recession rates at the TPS surface.

Two types of stress-based failure theories are available in the literature [19]: the maximum stress and the quadratic stress failure theories. In the maximum stress failure theory, the computed stresses are compared to the relevant material strength for each mode. Failure is predicted when the following criterion is satisfied:

$$\max\left(\frac{\sigma_{11}}{\sigma^{\mathrm{f}}_{\mathrm{t}1}}, \left|\frac{\sigma_{11}}{\sigma^{\mathrm{f}}_{\mathrm{c}1}}\right|, \frac{\sigma_{22}}{\sigma^{\mathrm{f}}_{\mathrm{t}2}}, \left|\frac{\sigma_{22}}{\sigma^{\mathrm{f}}_{\mathrm{c}2}}\right|, \frac{\sigma_{33}}{\sigma^{\mathrm{f}}_{\mathrm{t}3}}, \left|\frac{\sigma_{33}}{\sigma^{\mathrm{f}}_{\mathrm{t}3}}\right|, \left|\frac{\sigma_{12}}{\sigma^{\mathrm{f}}_{12}}\right|, \left|\frac{\sigma_{23}}{\sigma^{\mathrm{f}}_{23}}\right|, \left|\frac{\sigma_{31}}{\sigma^{\mathrm{f}}_{31}}\right|\right) > 1, \tag{9}$$

where $\sigma^{\mathrm{f}}_{\mathrm{t}i}$, $\sigma^{\mathrm{f}}_{\mathrm{c}i}$ are the maximum tension (t) and compression (c) material strengths in the three directions $i = 1,\ 2,\ 3$ and σ^{f}_{ij} with $i \neq \mathrm{j}$ are the shear strengths. Quadratic failure theories take into account the effective multi-axial loads on the material. Popular phenomenological failure theories for non-isotropic material are the Tsai-Hill and, more general, Tsai-Wu theories [20, 21].

The maximum stress model was chosen as a first approach for determining failing regions. Mechanical erosion is caused by brittle failure of the fibers, for which maximum stress theories work well. Additionally, it allows for easier identification of the responsible modes, essential for studying anisotropic materials. The uncertainties related to the maximum stress model still need to be evaluated. An extensive review and comparison of different failure prediction models can be found in [22], including ideas that might improve the predictive capabilities of this failure model.

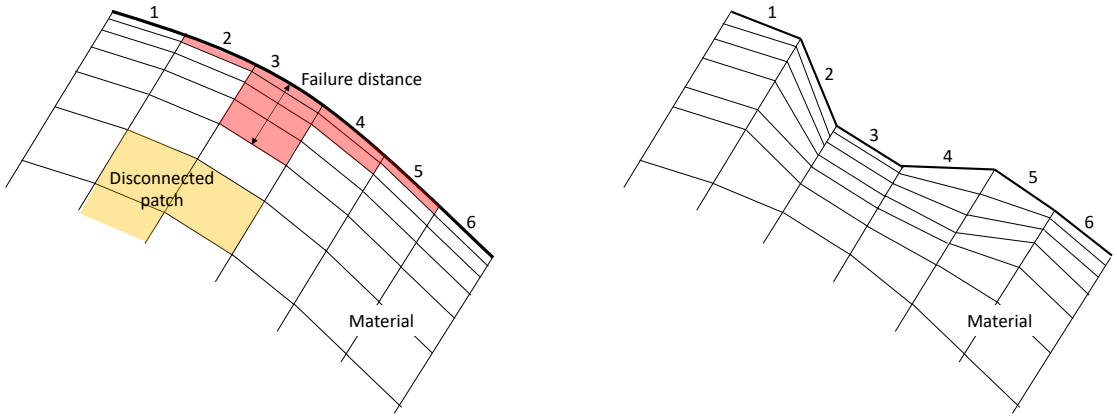

(a) Undeformed failing material. **(b) Deformed material.**

Fig. 1 Schematic for material failure.

D. Mass Removal Model

The failure criteria model gives for each computational cell the information of whether it is failing or not based on the stresses. In Fig. 1a, an example is given with the bold line defining the surface and the red and yellow failing cells. The difference between the two colors shows whether the topology of the failing region is connected to the surface. If the topology is not connected to the surface, such as the yellow region in Fig. 1a, the failing region is disregarded, since it involves mechanisms and phenomena, such as cracking, beyond the scope of this work. On the other hand, mechanical

erosion will appear at the failing faces adjacent to failing cells (faces 2, 3, 4, and 5 in Fig. 1a). The next step is to determine the failure distance, different for each failing face. The algorithm to compute the failure distance is split into two steps, a search starting from the surface to determine the first non-failing cell and a refinement to determine the exact distance. The search is performed perpendicularly to the surface inside the material with a geometrically increasing distance, checking the position of the first cell that is not failing. The precise location of the interface separating the failing to the non-failing region is then found with a bisection algorithm. The failure distance, l_f, is defined as the distance between the converged location of the interface and the face center coordinates. Assuming that the mechanical mass removal is faster than the time step, Δt, the recession rate, u_r, for each failing face is given as:

$$u_\mathrm{r} = \frac{l_\mathrm{f}}{\Delta t}, \tag{10}$$

The material grid is then deformed following the recession rates applied to all the failing faces using OpenFOAM dynamic mesh solvers, as shown in Fig. 1b. The deformed shape of the material will be the initial condition for the upcoming time step in both the thermal and the mechanical solver, for which the new failing region will be determined, and the procedure will be repeated.

The mass, m_f, removed from the material due to mechanical erosion during Δt is calculated for each face of area A as:

$$m_\mathrm{f} = \rho_s \, u_\mathrm{r} \, l_\mathrm{f} \, A \, \Delta t, \tag{11}$$

where ρ_s is the solid density.

III. Results

The final paper will include the results of a specific TPS test case following the methodology explained in Section II to analyze the potential mechanical erosion. Additional validation cases will be performed to ensure the accuracy of the stress analysis model implemented.

IV. Conclusion

This section will summarize the insights from the final paper after reviewing the results from the TPS mechanical erosion simulations. It will also include future work and ideas to extend the applicability of this study.

Acknowledgments

This work was supported by the NASA Entry Systems Modeling project (Michael Barnhardt project manager and Aaron Brandis principal investigator) as part of the NASA Game Changing Development program. The authors were funded by NASA contract NNA15BB15C to Analytical Mechanics Associates (AMA), Inc. and would like to thank John Thornton and Federico Semeraro for their insightful discussions on this work.

References

[1] Scala, S. M., and Gilbert, L. M., "Thermal degradation of a char-forming plastic during hypsersonic flight," *ARS Journal*, Vol. 32, No. 6, 1962, pp. 917–924.

[2] Mathieu, R. D., "Mechanical spallation of charring ablators in hyperthermal environments," *AIAA journal*, Vol. 2, No. 9, 1964, pp. 1621–1627.

[3] Schneider, P., Dolton, T., and Reed, G., "Mechanical erosion of charring ablators in ground-test and re-entry environments." *AIAA Journal*, Vol. 6, No. 1, 1968, pp. 64–72.

[4] Kratsch, K., Loomis, W., and Randles, P., "Jupiter Probe Heatshield Design," *18th Structural Dynamics and Materials Conference*, 1977, p. 427.

[5] Sullivan, J., and Kobayashi, W., "Spallation modeling in the Charring Material Thermal Response and Ablation (CMA) computer program," *22nd Thermophysics Conference*, 1987, p. 1516.

[6] Fu, R., Weng, H., Wenk, J. F., and Martin, A., "Thermomechanical coupling for charring ablators," *Journal of Thermophysics and Heat Transfer*, Vol. 32, No. 2, 2018, pp. 369–379.

[7] Lachaud, J., and Mansour, N. N., "Porous-material analysis toolbox based on OpenFOAM and applications," *Journal of Thermophysics and Heat Transfer*, Vol. 28, No. 2, 2014, pp. 191–202.

[8] Lachaud, J., Scoggins, J. B., Magin, T. E., Meyer, M., and Mansour, N. N., "A generic local thermal equilibrium model for porous reactive materials submitted to high temperatures," *International Journal of Heat and Mass Transfer*, Vol. 108, 2017, pp. 1406–1417.

[9] Meurisse, J. B., Lachaud, J., Panerai, F., Tang, C., and Mansour, N. N., "Multidimensional material response simulations of a full-scale tiled ablative heatshield," *Aerospace Science and Technology*, Vol. 76, 2018, pp. 497–511.

[10] Scoggins, J. B., and Magin, T. E., "Development of Mutation++: Multicomponent thermodynamic and transport properties for ionized plasmas written in C++," *11th AIAA/ASME joint thermophysics and heat transfer conference*, 2014, p. 2966.

[11] Whitaker, S., *The method of volume averaging*, Vol. 13, Springer Science & Business Media, 2013.

[12] Coman, C. D., *Continuum Mechanics and Linear Elasticity*, Springer, 2020.

[13] Demirdžić, I., Horman, I., and Martinović, D., "Finite volume analysis of stress and deformation in hygro-thermo-elastic orthotropic body," *Computer methods in applied mechanics and engineering*, Vol. 190, No. 8-10, 2000, pp. 1221–1232.

[14] Cardiff, P., Karač, A., and Ivanković, A., "A large strain finite volume method for orthotropic bodies with general material orientations," *Computer Methods in Applied Mechanics and Engineering*, Vol. 268, 2014, pp. 318–335.

[15] Weller, H. G., Tabor, G., Jasak, H., and Fureby, C., "A tensorial approach to computational continuum mechanics using object-oriented techniques," *Computers in physics*, Vol. 12, No. 6, 1998, pp. 620–631.

[16] Martin, A., Bailey, S. C., Panerai, F., Davuluri, R. S., Zhang, H., Vazsonyi, A. R., Lippay, Z. S., Mansour, N. N., Inman, J. A., Bathel, B. F., et al., "Numerical and experimental analysis of spallation phenomena," *CEAS Space Journal*, Vol. 8, No. 4, 2016, pp. 229–236.

[17] Grigat, F., Loehle, S., Zander, F., and Fasoulas, S., "Detection of Spallation Phenomena on Ablator Surfaces," *AIAA Scitech 2020 Forum*, 2020, p. 1706.

[18] Fu, R., Ramjatan, S., Kroells, M., Schwartzentruber, T., and Martin, A., "Micro-Scale Thermal-Structural Modeling for Carbon Fibers," *AIAA AVIATION 2020 FORUM*, 2020, p. 3273.

[19] Baker, A. A., *Composite materials for aircraft structures*, AIAA, 2004.

[20] Tsai, S. W., and Wu, E. M., "A general theory of strength for anisotropic materials," *Journal of composite materials*, Vol. 5, No. 1, 1971, pp. 58–80.

[21] Daniel, I. M., "Failure of composite materials," *Strain*, Vol. 43, No. 1, 2007, pp. 4–12.

[22] Soden, P., Hinton, M., and Kaddour, A., "A comparison of the predictive capabilities of current failure theories for composite laminates," *Composites science and technology*, Vol. 58, No. 7, 1998, pp. 1225–1254.